A&A 367, 170–182 (2001)
DOI: 10.1051/0004-6361:20000404

Astronomy & Astrophysics

The effect of rotation on the buoyant rise of magnetic flux tubes in accretion disks

U. Ziegler

Astrophysikalisches Institut Potsdam, An der Sternwarte 16, 14482 Potsdam, Germany

Received 18 September 2000 / Accepted 29 November 2000

Abstract. The dynamics of buoyant magnetic flux tubes in thin accretion disks is studied under isothermal conditions by means of numerical simulations. The influence of rotation on the rising behavior of the flux tube is examined and the role of a weak magnetic field line twist within the tube is investigated. By employing the adaptive mesh code NIRVANA the 3D simulations have effective resolution higher than in any previous numerical work on that topic. The fate of the flux tube strongly depends on the presence or absence of rotation respective differential rotation. Rotation effectively slows down the vertical ascend of the flux tube largely as a consequence of the Coriolis force acting on the surrounding flow which, in turn, reacts upon the tube. The detailed behavior also depends on the amount of twist. In accretion disks, a *weakly* twisted flux tube is disrupted and its rise is halted due to the impact of the magnetic shear instability which is driven by the interaction between the background rotational shear flow and (poloidal) twist field. As a consequence, the magnetic structure is captured in the inner disk region ($z < H_0$, H_0: disk scale height) a much longer time than suggested by the buoyant time scale in a non-rotating atmosphere. Untwisted accretion disk flux tubes do not break up quickly into pieces, as was found for corresponding tubes embedded in a non-rotating environment, but retain some degree of coherence albeit the stabilizing effect of twist is missing. In general, the numerical results are in gross contradiction to what postulates a highly simplified 1D picture based on the thin flux tube approximation.

Key words. MHD – instabilities – turbulence – magnetic fields

1. Motivation

Theoretical studies of the dynamical evolution of buoyantly unstable, isolated magnetic flux ropes are of importance in various astrophysical contexts and appear relevant for magnetically active stars like the Sun, disk galaxies as well as accretion disks:

Sun. Observations show that the solar surface magnetic field in active regions appears as a network of tube–like structures in which the magnetic flux is concentrated (Hughes 1992; Weiss 1994). Although theory lacks in details, these flux ropes are believed to have their origin in the undershoot layer where a dynamo replenishes the loss in magnetic flux through the combined action of differential rotation and turbulent convection (Wang & Sheeley 1991; Wang & Zirin 1991; Sheeley 1992). The dynamo–generated toroidal field may be subject to instabilities with the consequence that fragments of it break out (Matthews et al. 1995), become buoyant and rise through the convection zone as isolated flux ropes. To explain the observed appearance of the magnetic field one must therefore understand the manner in which such flux ropes ascend to the surface.

Send offprint requests to: U. Ziegler, e-mail: uziegler@aip.de

Galactic disks. The successfully used concept of isolated flux tubes in solar physics seems to be valuable also for galactic disks as an alternative means to explain dynamo action (α–effect). In classical mean field dynamo theory the α–effect is represented by correlations between interstellar turbulent motions and the magnetic field. Hereby it is assumed that fluctuations are small and the fields are distributed continuously over space (Krause & Rädler 1980). However, observations in our galaxy reveal that the magnetic field exhibits a very filamentary structure, especially on scales of 100 pc, rather than occupying the whole space (Heiles 1987; Heiles 1992). High–resolution observations of radio lobes associated with active galactic nuclei also show a highly structured morphology indicating a distribution of magnetic flux in form of ropes (Van Breugel & Formalont 1984). In such cases the mean field ansatz actually breaks down. It is then the task to try to model dynamo action directly from the observed intermittent field structure. In a likely scenario one can imagine that the flux ropes are formed as a result of the disruption of molecular clouds connecting pairs of cloud fragments (Hanasz & Lesch 1993). The flux ropes may then undergo the Parker instability and – due to the action of the Coriolis force – take on a characteristic

Ω–shape reminiscent of the behavior of cyclonic convective eddies.

Accretion disks. There is evidence from both analytical work (Kleeorin & Rogachevskii 1990) and direct numerical simulations (Horiuchi & Sato 1993) that, quite generally, turbulent plasmas have the tendency to organize the magnetic field into ropes or similar structures. Just recently, Ziegler & Rüdiger (2000) have shown in long–term simulations of the magnetic shear instability in accretion disks that the developing magnetic field is indeed preferably concentrated in ropes. Like in the case of galactic disks an alternative to statistical dynamo theory is thus to consider models based a priori upon the intermittent nature of the magnetic field. The simplest approach is to approximate such an inhomogeneous magnetic field as a collection of flux tubes. Although this is an idealized picture for the real situation, it may nevertheless describe to lowest order the scenario of a "flux tube accretion disk dynamo". To let such a dynamo work some mechanism must be present to prevent large buoyancy losses but which allows magnetic flux to be stored in the disk for a long enough time.

Due to its mathematical simplicity, the thin flux tube approximation (TFA) has gained great popularity in modeling the dynamics of magnetic flux tubes. In this approximation a flux tube is parameterized as a curve (tube axis) in space. The 3D MHD equations are reduced to a set of nonlinear equations describing the dependence of the variables along the curve as a function of time. Cross–sectional variations are neglected. Although the TFA has been applied with some success in problems dealing with wave propagation phenomena (Ulmschneider et al. 1991) or, for instance, in explaining observations of the latitudes of emergence and tilt angles of bipolar magnetic regions on the surface of the Sun (Fan et al. 1994; Caligari et al. 1995), fundamental difficulties remain. A more severe restriction concerns the interaction of the flux rope with the ambient medium. Usually, the back reaction of the surrounding gas is taken into account by an added inertia term suitable for flux tube motion in a potential flow. However, if the flow is more complex, as is expected in differentially rotating plasmas due to the action of tidal– and Coriolis forces, this simple description is no longer adequate so that the TFA may break down. To study the evolution of magnetic flux tubes in rotating systems one therefore has to solve the self–consistent 3D problem.

Numerical 3D flux tube dynamics is a task of considerable complexity facing the problem of resolving the small–scale flux tube in a large–scale structured environment. To date, most of the numerical 2D/3D calculations on flux tube dynamics have been done on uniform grids. The problem, however, may be treated with profit by means of adaptive mesh techniques. The use of an adaptive mesh refinement (AMR) algorithm can lead to a considerable reduction of computational costs compared to calculations performed on a uniform grid. The idea is to put resolution only where it is needed to resolve fine–scale structures in the flow and in the magnetic field. Further away from the flux tube a lower resolution is sufficient to describe the structures on larger scales.

The numerical experiments here, performed with a general–purpose 3D AMR–MHD code, aim to understand how buoyant, small–scale magnetic structures (flux tubes) evolve in non-turbulent accretion disks focusing on the effects of rotation and magnetic field line twist within the tube. In particular, we tried to give an answer to the yet open questions of flux tube coherence and storage of magnetic flux in the disk; important issues relevant for many dynamo scenarios. Moreover, the applicability of the thin flux tube approximation is checked in this context. The paper proceeds in the following way. In Sect. 2 the problem is formulated and the ansatz for its numerical solution using adaptive mesh techniques is discussed. The problem will be addressed step by step. As the first step results of non–rotating 2D models possessing slab symmetry are presented in Sect. 3. The 2D simulations do not only serve as reference for the 3D cases but can be compared with analogue computations for the solar convection zone. Results of 3D simulations are discussed in Sect. 4. Flux tube evolution for a non–rotating, uniformly rotating and differentially rotating (accretion disk) medium is examined separately to work out the various set in effects. The presented simulations should be considered as prototype calculations aiming on fundamental dynamical questions rather than playing around with the rich parameter space of the problem. Finally, conclusions are drawn in Sect. 5.

2. The model

2.1. Problem characterization

The problem of the rise of an isolated flux ring in a differentially rotating disk is simplified by employing the local box approximation. In cylindrical coordinates $\{R, \phi, z\}$ let us assume the angular velocity is given by $\mathbf{\Omega} = \Omega(R)\hat{\mathbf{z}}$ where $\hat{\mathbf{z}}$ is the unit vector in vertical direction. One considers then a rectangular patch of a disk located at a fiducial radius R_0 and solves the magnetohydrodynamical equations in a Cartesian coordinate system attached to the patch center. The coordinate axes are oriented in a sense that, locally, the unit vector $\hat{\mathbf{x}}$ points in radial direction and $\hat{\mathbf{y}}$ in azimuthal direction. Figure 1 schematically illustrates the local model in which the flux tube is a straight cylinder. In a co-rotating frame the following equations are to solve with $\Omega_0 = \Omega(R_0)$ as the angular velocity with respect to an inertial frame of reference:

$$\frac{\partial \rho}{\partial t} + \nabla(\rho \mathbf{v}) = 0, \tag{1}$$

$$\frac{\partial (\rho \mathbf{v})}{\partial t} + \nabla (\rho \mathbf{v}\mathbf{v}) = -\nabla p + \frac{1}{\mu}(\nabla \times \mathbf{B}) \times \mathbf{B} - 2\rho\Omega_0 \hat{\mathbf{z}} \times \mathbf{v} + 2\rho q \Omega_0^2 x \hat{\mathbf{x}} - \rho g \hat{\mathbf{z}}, \tag{2}$$

$$\frac{\partial \mathbf{B}}{\partial t} = \nabla \times (\mathbf{v} \times \mathbf{B}). \tag{3}$$

As usual, ρ is the gas density, p the gas pressure, $\mathbf{v}$ the fluid velocity and $\mathbf{B}$ the magnetic field. An isothermal equation

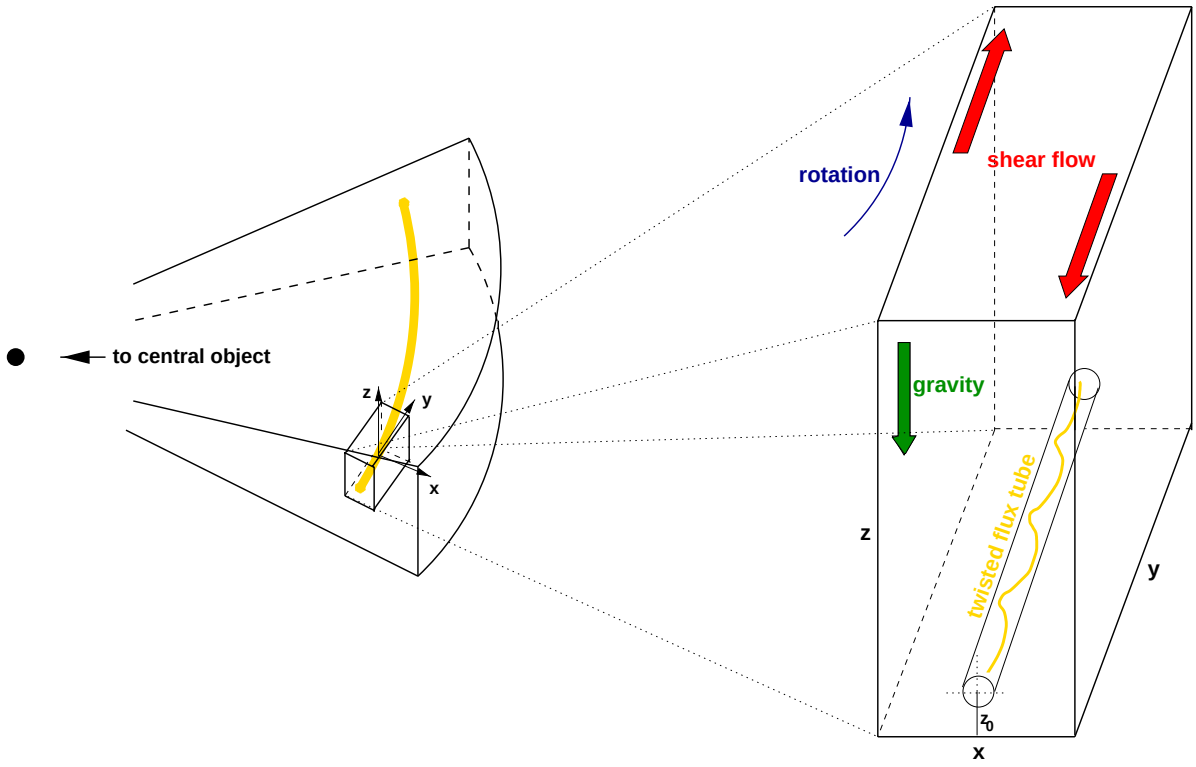

Fig. 1. Schematical illustration of the flux tube/accretion disk model

of state $p = c_{\rm S}^2\rho$ is assumed where $c_{\rm S}$ is the sound speed. $q = -{\rm d}\log\Omega/{\rm d}\log R|_{R_0}$ is a measure of the local shear rate derived from the rotation profile $\Omega(R)$ ($q = 1.5$ for a Kepler disk). The background rotational velocity in the co-rotating frame then is $\mathbf{v}(t=0) = -q\Omega_0 x\hat{\mathbf{y}}$ which describes a uniform shear flow in y–direction. The term $-\rho g\hat{\mathbf{z}}$ represents a vertical gravitational force with $g = g(z)$ being the force per unit mass. The $2\rho q\Omega_0^2 x\hat{\mathbf{x}}$ force term results from the expansion of the effective (gravitational+centrifugal) potential for $x/R \ll 1$. Ultimately, μ represents the magnetic permeability of the fluid which is set to the vacuum value $\mu = \mu_0 = 4\pi\ 10^{-7}$.

All simulations start with a buoyant magnetic flux tube placed in a stationary, non–magnetic atmosphere. Adopting $g = \Omega_0^2 z$ the vertical density distribution is given by the Gaussian profile

$$\rho_{\rm e} = \rho_0 \exp\left(-z^2/H_0^2\right), \tag{4}$$

where ρ_0 is the midplane density and $H_0 = (2c_{\rm s}^2/\Omega_0^2)^{1/2}$ is the disk scale height. The subscript "e" denotes external variables.

To link up with prior box simulations of magnetorotationally unstable accretion disks threaded by diffuse magnetic fields (Ziegler & Rüdiger 2000), dimensionless parameters are used: $\rho_0 = 1$, $\Omega_0 = 10^{-3}$, and $H_0 = 1$. The value for Ω_0 corresponds to a radius $R_0 = 100$ if one arbitrarily sets $GM = 1$, where G denotes the gravitational constant and M is the mass of the central object in an accretion disk.

Next, the magnetic flux tube is constructed and matched to the atmosphere. In a cylindrical coordinate system $\{\tilde{R}, \tilde{\phi}, \tilde{z}\}$ anchored in the tube with tube radius $\tilde{R}_{\rm t}$ and with the tube axis as $\tilde{z}$–axis the adopted magnetic field reads:

$$\begin{pmatrix} B_{\tilde{R}} \\ B_{\tilde{\phi}} \\ B_{\tilde{z}} \end{pmatrix} = \begin{cases} \begin{pmatrix} 0 \\ \xi\tilde{R}/\tilde{R}_{\rm t} B_{\tilde{z}} \\ B_0\left(1-\tilde{R}^2/\tilde{R}_{\rm t}^2\right)^p \end{pmatrix} & \text{for } \tilde{R} \le \tilde{R}_{\rm t} \\ \mathbf{0} & \text{for } \tilde{R} > \tilde{R}_{\rm t}. \end{cases}$$

The field strength drops off with radius at a rate depending on the exponent p. The rate of twist is determined by the parameter ξ which is connected to the pitch angle $\theta = \tan^{-1}(B_{\tilde{\phi}}/B_{\tilde{z}}) = \tan^{-1}(\xi\tilde{R}/\tilde{R}_{\rm t})$. As noted in Linton et al. (1998), flux tubes with such field profiles are unstable due to the kink instability only if $\xi > p^{1/2}$. Such a priori kink–unstable tubes are not considered here but this study is restricted to flux tubes possessing a weak twist. In the present sample of simulations $p = 0.5$ and $\xi = 0.17$ ($\theta_{\rm max} \approx 10^\circ$ at $\tilde{R} = \tilde{R}_{\rm t}$) or $\xi = 0$ (untwisted tubes).

In the Cartesian simulation domain, the flux tube axis is oriented parallel to the y–axis and located a distance $z_0 = 2.5\tilde{R}_{\rm t}$ above the midplane (see Fig. 1). The y(longitudinal)–component of the magnetic field is given by $B_y(x,z) = B_{\tilde{z}}(\tilde{R}(x, z-z_0))$ with $\tilde{R} = (x^2+(z-z_0)^2)^{1/2}$. For numerical reasons B_x and B_z are computed from the vector potential component

$$A_y = \frac{1}{2}\frac{\xi}{p+1}\tilde{R}_{\rm t} B_0 \left(1-\frac{\tilde{R}^2}{\tilde{R}_{\rm t}^2}\right)^{p+1}$$

(i.e. $B_x = \partial A_y/\partial z$ and $B_z = -\partial A_y/\partial x$) to ensure that the magnetic field is divergence–free on the mesh. Of course, the resulting transverse field is identical to the twist field, $\mathbf{B}_\perp = B_x\hat{\mathbf{x}} + B_z\hat{\mathbf{z}} = B_{\tilde{\phi}}\mathbf{e}_{\tilde{\phi}}$, where $\mathbf{e}_{\tilde{\phi}}$ is the azimuthal unit vector in the tube cylindrical coordinate system.

The field configuration is not force–free and a pressure gradient within the tube is necessary to compensate the Lorentz force. Equilibrium is achieved by calculating the pressure inside the tube from the relation

$$p = p_\mathrm{e} - \frac{1}{2\mu}\left(B_\perp^2 + B_y^2\right).$$

The internal density then follows from the isothermal assumption i.e. $p/\rho = p_\mathrm{e}/\rho_\mathrm{e}$. Consequently, $\rho < \rho_\mathrm{e}$ and the flux tube experience buoyancy.

It should be noted that, because of the staggered grid discretization in the finite–difference code, *numerical* equilibrium is not exactly fulfilled. It is the $B_\perp^2/(2\mu)$ part of the magnetic pressure which is difficult to bring into numerical force balance. However, for weakly twisted tubes ($B_\perp^2 \ll B_y^2$), as regarded here, the resulting "numerical force" from the small imbalance has very little dynamical effect.

To complete the characterization of the problem it remains to specify the radius of the flux tube $\tilde{R}_\mathrm{t}$ and the strength of the magnetic field B_0. In all simulations, $\tilde{R}_\mathrm{t} = 0.04$ (remember that the scale height $H_0 = 1$) and $\beta = 2\mu p(\tilde{R}=0)/B_0^2 = 0.5$ (i.e. $B_0 = 9.084\ 10^{-7}$). Note that, albeit $\tilde{R}_\mathrm{t} \ll H_0$, the flux tube can not be regarded as *thin* in the sense of the TFA because of considerable radial variations in the density, pressure and magnetic field.

2.2. Computational ansatz

The simulations are performed with the adaptive mesh MHD code NIRVANA[1] developed by the author over the last years (Ziegler & Yorke 1997; Ziegler 1998; Ziegler 1999). NIRVANA uses a hierarchy of refinement levels $\ell = 1...\,L$ such that the mesh spacing is halved when going from level ℓ to the next higher level $\ell + 1$. Refinement is done recursively starting on a basic grid with mesh spacing $\delta x^{(0)}$. For a high degree of flexibility, a refinement level is comprised out of smaller entities – patches of size $4\times4(\times4)$ numerical cells – arranged according to resolution requirements.

Numerical gradient values of all fluid variables are taken as indicator for mesh refinement. The grid refines, if one of these (normalized) values exceeds a given threshold ϵ:

$$\frac{|\delta f|}{|f| + f_\mathrm{ref}}\left(\frac{\delta x^{(\ell)}}{\delta x^{(0)}}\right)^\nu > \epsilon, \qquad f = \{\rho, v_i, B_i\}.$$

$\delta x^{(\ell)}$ denotes the mesh spacing of the ℓth level and $f_\mathrm{ref} \geq 0$ is a reference value to keep the denominator in the expression well defined. In the present study $\epsilon = 0.1$ and $\nu = 1 - \ell/5$ which controls grid refinement. To have a concrete situation in mind, refinement on the basic grid (1st–level) takes place, for example, if the relative density change $\delta\rho/\rho$ exceeds a value of 0.1 (0.174). The choice of refinement parameters makes sure that the flux tube initially is resolved with the maximum refinement level L which has been restricted to $L = 2$ because the simulations are still very CPU time consuming. Hence, on the finest level one ends up with an effective resolution of $256 \times 512 \times 512$.

If not otherwise stated, the 3D basic grid is represented by $64 \times 128 \times 128$ grid points and spans a physical volume of $(x, y, z) \in [-0.5, 0.5] \times [0, 2] \times [0, 2]$. Reflecting boundary conditions are used in x–direction, periodic boundary conditions in y–direction and reflecting (bottom) respective outflow (top) conditions in z–direction.

3. Two–dimensional simulations

The 2D (x, z) simulations start with a flux tube of cylindrical shape sitting in an isothermal atmosphere with Gaussian density distribution. The stratification is appropriate for a thin accretion disk. For the present, differential rotation of the disk is ignored. Slab symmetry is assumed along the y(azimuthal)–direction. This simplified non-rotating model has been investigated for three reasons. First, it serves as a reference for the more complicated 3D calculations presented in Sect. 4. Second, it seems useful to compare the results with solar convection zone flux tubes which are well studied objects in the literature. Differences in the evolution are expected because of the different types of stratifications employed. The pressure contrast between the top and bottom of our disk atmosphere, which spans two scale heights, is ≈53. This is significantly larger than in typical convection zone flux tube simulations. Moreno-Insertis & Emonet (1996) report a pressure contrast of 2.6 in their models using an adiabatically stratified atmosphere. Hughes & Falle (1998) performed 2D adaptive mesh simulations in a background medium with pressure contrast ≈10. Besides the stratification of the background medium, the tube plasma–β is another important difference. In our simulations the maximum β (=0.5) is much smaller than the values typically found in solar convection zone models (of order several tens or hundreds). Thus, under isothermal conditions as assumed here, accretion disk flux tubes are much more buoyant than convection zone flux tubes because of the larger density deficit, $(\rho_\mathrm{e} - \rho)/\rho = 1/\beta$, in accretion disks. Third, the power and functioning of the adaptive mesh algorithm is demonstrated by comparing the 2D AMR results with computations performed on a high–resolution, uniform grid. Because of severe restrictions in computer power such a comparison is not possible for the 3D simulations.

Figure 2 shows a snapshot series revealing the time evolution of a weakly twisted ($\xi = 0.17$) flux tube. For later comparison, the time is measured in units of $2\pi/\Omega_0$ – the fictitious rotation period at the fiducial radius R_0 of

[1] For more information about the code see `http://www.aip.de/~ziegler`

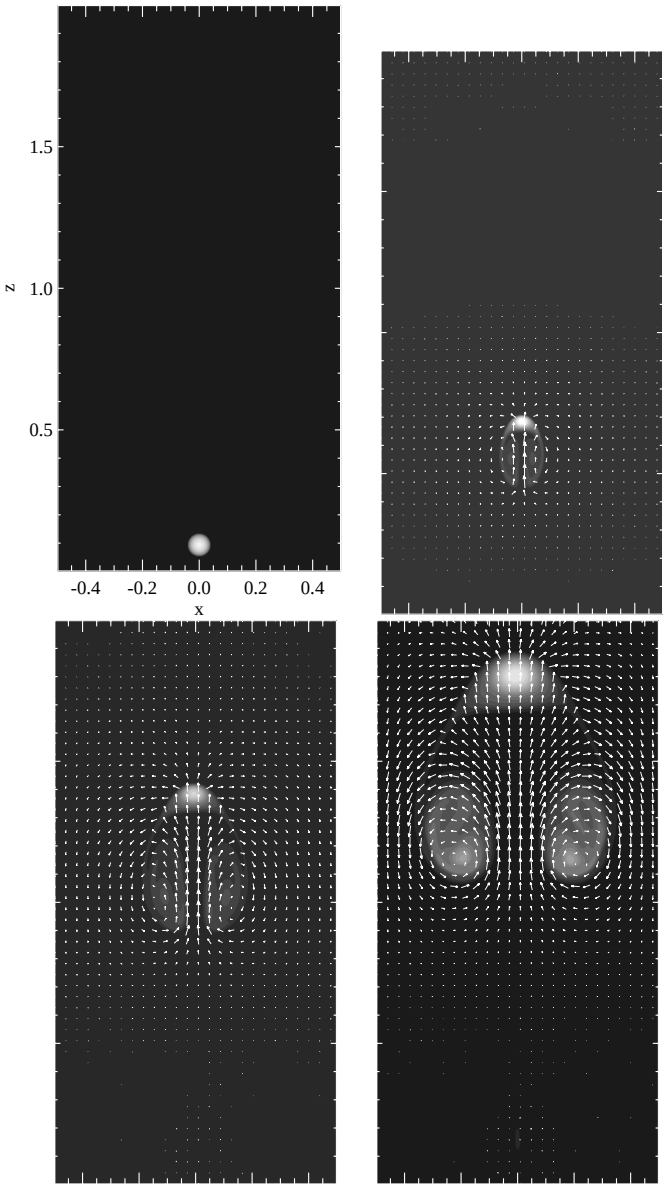

Fig. 2. Series of snapshots at times $t = 0, 0.97, 1.73, 3.66$ showing the distribution of B_y (grey–scale images) and the velocity field (arrows). In each plot the magnetic field is individually scaled from a minimum value ≈ 0 (dark tones) to $B_{y,\max} = (1, 0.65, 0.17, 0.05) \cdot B_0$ (light tones). The largest arrow corresponds to a velocity of 1.2 10^{-4} ($\approx 0.17 c_s$)

the disk. In this time unit the simulation has been stopped after 3.66 "orbits". The initial stage of evolution is characterized by the formation of a tube head accompanied by two sidelobes. In regions where the magnetic energy density of the transverse field component is below the kinetic energy density of the flow magnetic flux is peeled off the tube. The magnetic flux is advected from the vorticity boundary layer around the head surface (Fig. 3, left panel) into the wake that forms behind the tube head hereby taking along vorticity, $\omega_y = (\nabla \times \boldsymbol{v})_y$. Note that the remaining vorticity components are small compared to ω_y. The thickness of the vorticity layer is approximately 1/20 to 1/10 of the head diameter. A related thin current density layer (Fig. 3, right panel) has comparable thickness to the vorticity layer. The current layer almost completely encloses the tube head with stronger currents occurring at the front. The layer is disconnected at the lower left and lower right corner of the tube head and extends far into the wake forming a pipe–like filament on either lateral side. The current–carrying pipes provide a channel through which the peeled magnetic flux is transfered to the wake.

The fine structure seen in the close–up view Fig. 3 is likely sensitive to the amount of diffusivity in the problem as well as the accuracy of representation of the initial structure within the flux tube. Although physical resistivity is not included in the model, the results may suffer from numerical diffusion due to truncation errors in the code. The level of numerical diffusion, in turn, depends on the resolution. In effect, the solution may not converge to the true ideal MHD solution. This can be checked by a resolution study. In the lower panels of Fig. 3, the vorticity and current density is also shown for a higher resolved run ($L = 3$, effective resolution: 512×1024). In addition, the $L = 3$ AMR run has been verified with a high–resolution single grid run which essentially gives the same results. Note first that it makes little sense to perform lower resolved runs because of poor representation of the initial flux tube structure. In the higher resolved cases the thickness of the boundary layers is smaller as might be expected. The rope–like magnetic filaments turn out to be unstable and become wiggled in the course of flux tube rise. Note that the corresponding evolution time is not the same as that for the $L = 2$ simulation. In particular, the flux tube head in the $L = 3$ run reaches the same height at an earlier time. Hence, not only the details of dynamics but the rising behaviour of the flux tube depend on resolution. This is a somewhat unsatisfactory situation, but unfortunately, the 3D simulations which follow are restricted to a maximum refinement level of $L = 2$ because of severe time limitations. The final results should therefore be interpreted with some caution keeping in mind the possible dependence on numerical resolution.

At later times a significant amount of magnetic flux has been accumulated in the wake. More specifically, about 65 percent of the initial flux has been transfered to the wake at the end of the simulation. This is a relative high quota compared to convection zone flux tubes explicable by the stronger density decline per scale height in the accretion disk atmosphere. Most of the flux lost from the tube head reside in two egg–shaped magnetic structures which can be thought as the remnants of the initial sidelobes and which have largely separated from the tube head. These magnetic structures are enclosed by counter-rotating larger–scale eddies.

The structure of the transverse magnetic field (arrows) and longitudinal velocity component v_y (grey–scale plot) at time instant $t = 3.66$ is illustrated in Fig. 4. The (anticlockwise rotating eddy has a small (positive) negative longitudinal velocity component which means that both vortices have helical structure. The sense of screwness is

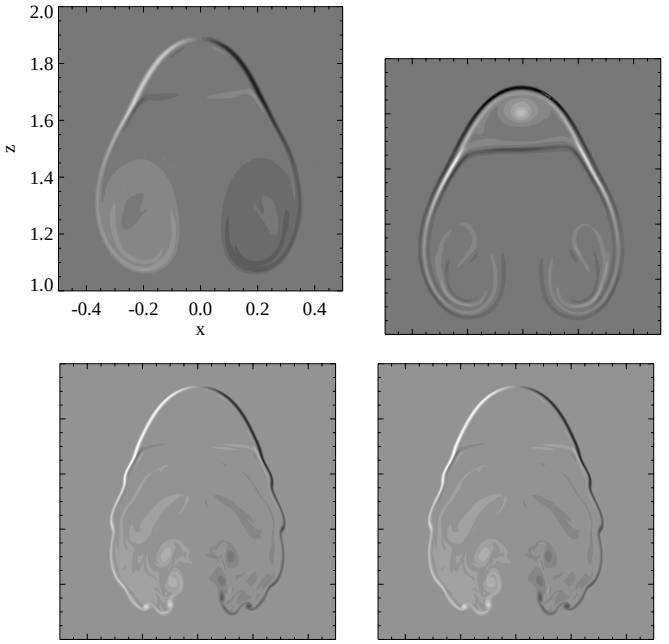

Fig. 3. Upper left: grey–scale plot of the y–component of vorticity $\boldsymbol{\omega} = \nabla \times \boldsymbol{v}$ at time $t = 3.66$. Scaling is linear from $-\omega_{\max}$ (darker) to $\omega_{\max}$ (lighter) where $\omega_{\max} > 0$ is the maximum value of vorticity at that time. Upper right: grey–scale plot of the y–component of $\nabla \times \mathbf{B}$ at $t = 3.66$ linearly scaled in the same way as the vorticity. Lower panels: the same quantities as in the upper panels but for a $L = 3$ AMR run and shown at time $t = 2.85$

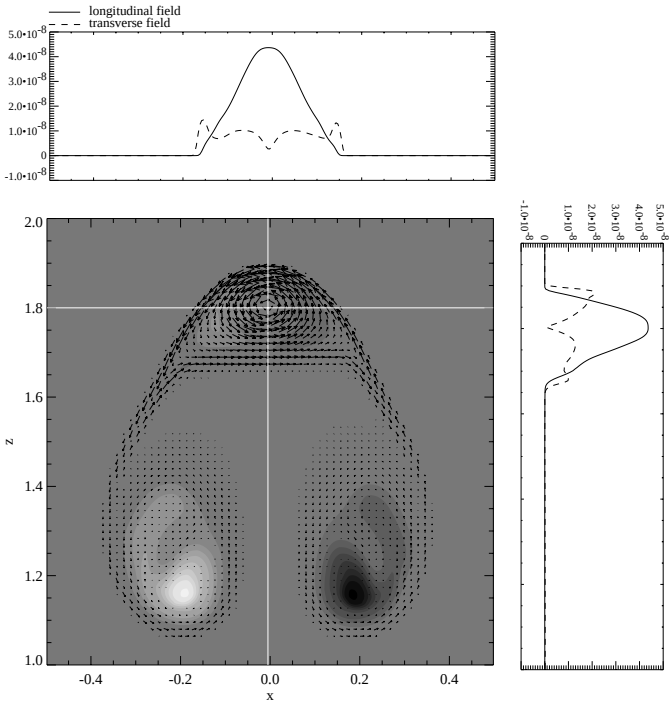

Fig. 4. Structure of the transverse magnetic field (arrows) and grey–scale image of v_y at $t = 3.66$. The maximum arrow length corresponds to a field strength of $0.023 \cdot B_0$. v_y is linearly scaled from $-v_{y,\max}$ (darker) to $v_{y,\max} = 4.9\ 10^{-5} \approx 0.07 \cdot c_{\rm S}$ (lighter). The side plots show the variation of B_y respective $|\mathbf{B}_\perp|$ along the curves $z = 1.8$ and $x = -0.005$

the same for both vortices. A careful analysis of the data reveals that y–momentum is not generated in the wake but near the tube surface due to a small magnetic force in y–direction resulting from the distortion of the cross–section of the tube head. y–momentum is then advected downwards through the pipes and mixed with the ambient medium. The total y–momentum is consistent with zero as it is expected from conservation principles.

The side plots in Fig. 4 show the variation of B_y respective transverse field strength $|\mathbf{B}_\perp|$ along the two curves $z = 0$ and $x = -0.005$ crossing the center of the tube head defined here as the location where B_y peaks. Although the flux tube is initially stable to kink perturbations this may change during its ascend. Because of the strong vertical gradient in the atmospheric density the cross–section of the tube expands when it rises accompanied by a decrease in the strength of B_y. At the latest time, the head of the tube has a diameter about twice as large as at the beginning and B_y has decreased to a maximum value of $B_{y,\max} = 0.05 \cdot B_0$ measured in the center of the tube head. The key point is that the change in B_y is not necessarily in proportion to the decrease in the transverse field (Kuznetsov & Hood 1997). Consequently, the field line pitch may increase making the tube head more prone to the kink instability. The tube is kink unstable for pitch angles exceeding a critical one whose value depends on the radial magnetic field profile. The critical pitch angle for our magnetic field configuration measured at the tube radius is $\theta_{\rm crit} \approx 35°$ (Linton et al. 1998). It is seen from the side plots that most of the head volume is clearly stable against kink perturbations. The criterion for kink stability is only violated in a narrow layer around the surface. In this layer, relative large pitch angles of $\theta > 45°$ occur which are above the critical value. Supercriticality is pronounced at the front of the tube head surface due to the fact that the transverse field is compressed there. It is unclear whether the adjusted pitch angle distribution involves important dynamical consequences for the flux tube as a whole. This is because, being a 3D phenomenon, the kink instability can not be studied with the present 2D model. Possible 3D effects are therefore investigated in Sect. 4.1 by means of a three–dimensional extension of the 2D model.

Figure 5 (right panel) shows the final state ($t = 3.66$) of an untwisted ($\xi = 0$) flux tube. The vertical rise of the flux tube quickly ceases and the tube splits into two pieces. The fragments essentially move in horizontal direction and they are enclosed by vortices spinning with opposite circulation. The fragments are still buoyant but the buoyancy force is compensated by a hydrodynamic side force experienced by the translating vortices. This lift force is exerted on an object moving translationally while carrying around it a net circulation (Saffman 1992). The observed fragmentation is due to a torque on the flux tube produced by the buoyancy gradient within the flux tube and is due to pressure forces at the tube surface exerted by the

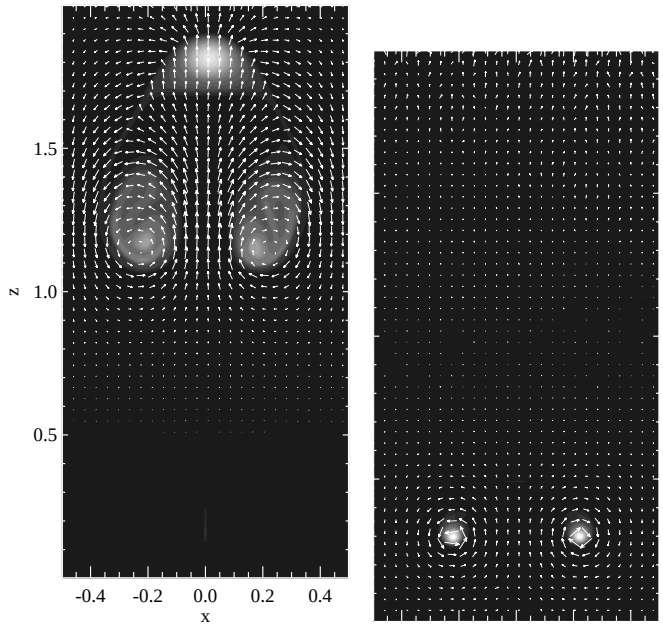

Fig. 5. Similar snapshots ($t = 3.66$) to Fig. 2 for a twisted tube simulation on a uniform grid with resolution 256×512 (left) and an untwisted tube adaptive mesh model (right)

external medium. A sufficient transverse magnetic field component missing here has a stabilizing effect on this disruptive process as demonstrated before. In the twisted tube case the magnetic tension force which arises when the cross–section of the tube is deformed counteracts the distorting impact of buoyancy gradients. The finding that the process of fragmentation or non–fragmentation depends on the rate of magnetic field line twist is strongly reminiscent of model computations of flux tubes in the solar convection zone (Schüssler 1979; Longcope et al. 1996; Moreno-Insertis & Emonet 1996; Emonet & Moreno-Insertis 1996; Fan et al. 1998; Emonet & Moreno-Insertis 1998; Dorch et al. 1998).

As a check for the adaptive mesh calculation, Fig. 5 (left panel) shows a snapshot at $t = 3.66$ of an analogue twisted flux tube model performed with a uniform grid of 256×512 grid points ie. it has globally the spatial resolution obtained at most locally in the AMR case. There is obviously a rather good agreement between both simulations (compare Fig. 5 with Fig. 2). A more detailed inspection suggests minor differences, for example, in the velocity field structure around the initial flux tube location. In summary, however, the AMR method has been proven to be an adequate and powerful tool for this class of problem: averaged over the entire simulation, the gain in performance using AMR instead of a uniform grid is about 14 (22) for the twisted (untwisted) tube case.

4. Three–dimensional simulations

4.1. The non–rotating case

Having demonstrated that the adaptive mesh code works well, the focus is now turned to the more interesting and more realistic three–dimensional evolution relaxing at first the constraint of slab symmetry. That is, the y(azimuthal) direction is added to the computational domain. The same initial configuration is used as in the 2D run. In particular, differential rotation has been ignored again. Two major physical effects may influence the dynamics of the flux tube. That is the kink instability and the Parker instability. The first of these concerns flux tubes possessing a sufficient amount of twist. Conserving the total magnetic helicity (non-resistive case), the effect of the kink instability is to convert twist into writhe thereby deforming a straight flux tube into a helical tube (Fan et al. 1998). The Parker instability is independent from the presence of tube twist but just requires a lower density magnetic layer in a gravitational field. As first shown by Parker (1974), the curvature of a vertically perturbed horizontal magnetic field may be too small for magnetic tension to balance the destabilizing effect of buoyancy. In case of a thin, untwisted flux tube in a thin accretion disk this happens for perturbations with wavelengths larger than the critical value $\lambda_{\rm crit} = 2\pi H_0$ (Schramkowski & Achterberg 1994). As a result of the instability, the magnetic flux tube is expected to arc. In this study, however, the Parker instability does not play any role. This is because the dimensions of the computational domain are chosen that the Parker instability is suppressed from the beginning. Recall that the maximum dimension of the computational box is $2H_0 < \lambda_{\rm crit}$ which is less than the critical wavelength by a factor of π.

The prior 2D model showed that during the tube's ascend a boundary layer satisfies the criterion for the onset of the kink instability. On the hand hand, the inner region of the flux tube head has been proven to be kink–stable. The outcome of the 3D simulation yields that the flux tube remains kink–stable all the time during its ascend. Moreover, apart from small azimuthal variations seen in the flow structure no significant 3D effects are observed at all. Hence, the evolution of the flux tube goes in the same manner as presented in the 2D simulation. However, differences may occur in the subsequent evolution going beyond the time simulated here. There might be still a chance for the flux tube to kink when it enters deeper into the low–density outer atmosphere. The pitch angle may further increase and the unstable region may cover a larger and larger volume fraction of the flux tube head which, ultimately, will cause the tube head to kink as a whole.

4.2. The effect of uniform rotation

As has been demonstrated in the non-rotating 2D and 3D models the rising behavior of flux tubes is determined by the buoyancy force counteracted by the resistance of the surrounding medium. In this exemplary simulation the previously adopted constraints are further relaxed by allowing the background medium to rotate with a constant angular velocity Ω_0. In case of a uniformly rotating

background medium the surrounding flow and, consequently, the pressure distribution around the flux tube is influenced by the Coriolis force. Hence, the wake structure is expected to be modified by rotational effects. Also, the reaction force of the external medium upon the flux tube changes which, in turn, modifies the rise speed of the flux tube. The influence of rotation can be parameterized by the ratio of the buoyancy time scale, τ, computed for the case as if there were no rotation present, to the rotation period, $2\pi/\Omega_0$. For slowly rotating atmospheres like that of the Sun ($\tau \ll 2\pi/\Omega$) the effect of rotation may be negligible. But in accretion disks τ is comparable to the rotation period ($\tau \propto \Omega_0^{-1}$ because of $g = \Omega_0^2 z$) which can be verified directly from the non-rotating simulations. One therefore expects the dynamical evolution of a flux tube to be significantly modified in an accretion disk. Before turning to the detailed rising behavior of the flux tube note first that, to a very good approximation, the developing magnetic structure maintains its initial slab symmetry and remains quasi–horizontal. Only small deviations from slab symmetry are observed which do not represent any features worth to mention.

Figure 6 presents a close–up view of the magnetic field structure (left panel) and flow structure (right panel) at time $t = 2.67$. Slices at $y = 0$ through a subdomain of the total computational box are shown. The overall flux tube evolution is quit different from that of the non-rotating case. Major points concern the structure of the wake and magnetic field, and the rising behavior of the flux tube. As the flux tube starts to ascend the production of sidelobes as found in the non-rotating case does not take place. A vortex pair different in nature to the vortices generated in the non-rotating model develops and lags behind the tube head. The eddies, which have a dimension comparable to or somewhat larger than the head diameter, have opposite circulation and carry an axial flow which is negative in the vortex on the $x < 0$ side and positive in the vortex located on the $x > 0$ side. These vortex pair is a direct consequence of the interaction of the flow induced by the tube's vertical motion and the Coriolis force. The vortex pair thus vertically moves in accordance with the tube head. Note that the vortices have opposite helicity to the magnetic field carrying vortices occurring in the non-rotating environment (compare Fig. 6 with Fig. 4; in Fig. 4 the sign of v_y must be reversed for this comparison because, actually, the 2D model were calculated in a left–handed coordinate system). This underlines the different natures of vortex generation in the uniformly rotating case here and non-rotating case.

The observed vortex pair plays an important role in structuring the wake that forms behind the flux tube head. The vortices act like collimating rolls which channel the magnetic flux peeled off from the tube surface and suppress the formation of sidelobes. That makes the magnetic wake to appear in a comet–like shape. The loss of magnetic flux from the tube head is less severe than in the case without rotation. Approximately 65% of the total magnetic flux is concentrated in the tube head. The rest is contained in the wake. A vortex street has developed in the wake which is characterized by a few smaller eddies having an alternating sense of circulation.

The Coriolis force has large influence on the expansion of the tube's cross–section during its ascend in lower density regions. As can be seen from Fig. 6 (right panel) there is an axial velocity component in front of and lateral to the flux tube head which is positive on the left side ($x < 0$) and negative on the right side ($x > 0$). The Coriolis force resulting from this velocity component is directed toward the plane $x = 0$ and counteracts the expansion of the tube head caused otherwise by the decrease in external density. At $t = 2.67$ the diameter of the tube head is still comparable to the initial flux tube diameter. The maximum field strength in the tube head has decreased to a value $B_{\max} \approx 0.58 B_0$. This is a factor of $\approx$6 larger than in the non-rotating case at the same time instant. In contrast to the latter, where the weakening of the magnetic field is in part by the decrease in the external pressure and in part due to the peeling effect, here magnetic flux peeling is the relevant process leading to the decrease in the field strength of B_y.

Another apparent effect of the Coriolis force is the reduction of the rise speed of the flux tube. Although there is no direct influence on the vertical tube motion ($\boldsymbol{\Omega} \parallel \hat{\boldsymbol{z}}$), the Coriolis force acts to modify the pressure distribution around the flux tube in a sense that the pressure difference between the front and rear of the tube head is increased. The excess force is directed downwards and slows down the vertical motion of the tube head (see also Sect. 4.4).

4.3. Flux tube evolution in a Keplerian shear flow

In a next step the evolution of a magnetic flux tube in an accretion disk environment is studied. The model is distinct from the previous uniformly rotating case by adding a background shear flow, $v_y = -q\Omega_0 x \hat{\boldsymbol{y}}$. The presence of differential rotation adds new complexity to the problem because of possible implications resulting from the magnetic shear instability (MSI). As demonstrated analytically by Balbus & Hawley (1991) a differentially rotating plasma with outward decreasing angular velocity, $\mathrm{d}\Omega/\mathrm{d}R < 0$ ($\Omega \propto R^{-1.5}$ in a Kepler disk), is dynamically unstable when threaded by a weak, subthermal magnetic field. There is extensive literature devoted to numerical simulations of the MSI for magnetic field configurations continuously distributed over space (Hawley et al. 1995; Brandenburg et al. 1995; Abramowicz et al. 1996; Stone et al. 1996; Hawley et al. 1996, Hawley & Stone 1998; Ziegler & Rüdiger 2000). But, to date, there is no three–dimensional numerical study examining the case of intermittent field structures like those considered here in form of magnetic flux tubes. This is mainly because of a lack in resolution needed to represent the small–scale magnetic field of a flux tube which is embedded in a large–scale structured atmosphere. Here, this scaling problem

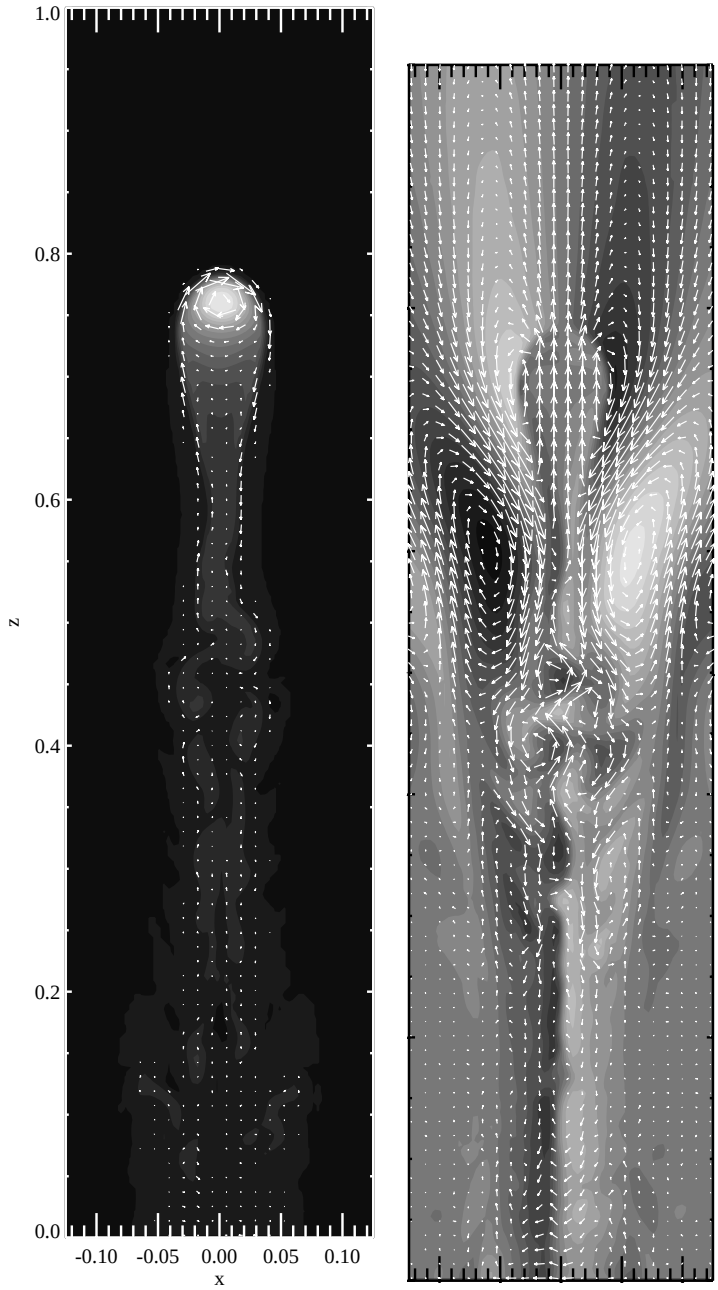

Fig. 6. Magnetic field structure (left) and flow structure (right) for the uniformly rotating case at $t = 2.67$. In both plots the axial component is represented by the grey–scale image whereas the arrows show the transverse vector component

is accounted for using the technique of adaptive mesh refinement.

Having knowledge about the existence and properties of the MSI the dynamical behavior of a buoyant flux tube in an accretion disk is expected to depend on the presence or absence of twist. Untwisted tubes with a weak ($\beta > 1$), purely longitudinal magnetic field are unstable against non-axisymmetric perturbations but with growth times of tens of orbital periods (Balbus & Hawley 1992). In our simulations β increases with distance from $\beta = 0.5$ at the tube axis to infinity at the tube radius. Thus, a cylindrical core region around the tube axis is stable whereas the rest of the tube volume is unstable. However, since the simulated evolution times are restricted to a few orbits and the expected growth times are relatively larger, the MSI should play, at least initially, no role in the dynamical evolution of untwisted flux tubes. This does not exclude that the MSI may also become important during the evolution, if a poloidal magnetic field component is produced.

The situation is quite different for tubes possessing a *weak* magnetic field line twist. The presence of such a poloidal field component render growth rates much larger than in the non–twisted case with e–folding times measured now in fractions of an orbital period (Balbus & Hawley 1991). It may then be expected that, unlike for

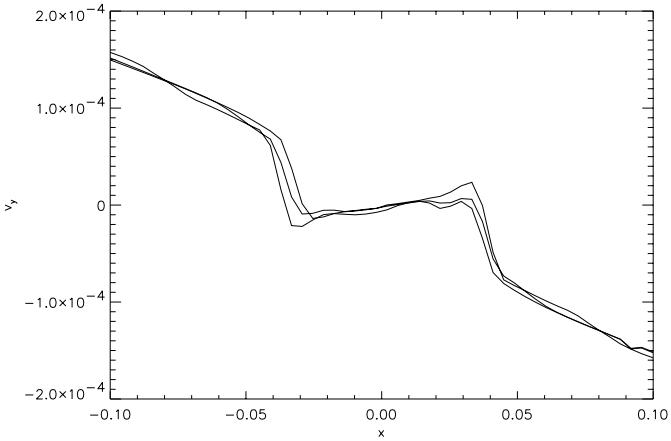

Fig. 7. v_y–profile along a line parallel to the x–axis through the tube center and at $y = 1$ for 3 subsequent times $t = 0.55, 1.09, 1.54$

tubes without twist, the MSI will have significant influence on the flux tube dynamics after few rotational periods.

The results of two simulations are discussed. The first considers a flux tube with weak twist ($\xi = 0.17$). In the second, an initially untwisted tube ($\xi = 0$) is assumed. To reduce boundary effects, the dimension of the computational domain has been extended to $[-0.75, 0.75] \times [0, 2] \times [0, 2]$ using a basic grid of $96 \times 128 \times 128$ cells. It is started with the twisted tube case. The initial phase of evolution $t \lesssim 0.3$ is similar to all other models and is determined by the start–up buoyancy force. From the beginning the background shear stretches the radial component of the poloidal magnetic field. Because of the assumed field topology, field line stretching reduces the strength of the longitudinal magnetic field in the tube half above the tube center (the location where B_y peaks) and strengthens it below. The resulting magnetic force produces a longitudinal flow in a manner to compensate shear inside the tube. The effect is illustrated in Fig. 7 where for different times the v_y–profile is shown along a line parallel to the x–axis and crossing the center of the flux tube. One sees that v_y slightly increases with x within the tube contrary to the overall background shear. Note the transition layer with strong velocity gradient at the tube surface. The excess in v_y means that a Coriolis force is exerted on the flux tube. This force is directed in $(-x)$–direction on the left tube side $x < 0$ and in $(+x)$–direction on the right tube side $x > 0$ and tries to separate both tube sides horizontally. On the other hand, the twist field stabilizes the tube against any deformation of the cross–section because of magnetic surface tension. In effect, the tube is not split but somewhat elongated in x–direction. The resulting increase in resistance slows down the vertical tube motion by a small amount (see also Sect. 4.4).

The MSI does not operate in the whole interior of the flux tube because the criterion of outward decreasing angular velocity is not fulfilled as can be derived from Fig. 7. However, the MSI is active in the transition layer where strong negative gradients occur. At later times, the MSI enters the non–linear regime and becomes a dominant factor in the dynamics of the flux tube. Figure 8 illustrates the final stage of evolution for the twisted flux tube. The snapshot is taken at $t = 3.51$ and shows the spatial location of the magnetic energy for field strength $|\boldsymbol{B}| > B_{\max}/2$, where $B_{\max}$ is the maximum field strength in the box at the given time. The structure of the resulting flow in a slice through the computational domain at $y = -0.6$ is overplotted. Note that in this plot the shear (y–)component, v_y, has been artificially set to zero to emphasis the transverse part of the velocity field. Otherwise the larger shear component would hide the details in the flow around the resulting magnetic structure. In contrast to the evolution of a flux tube in a non-rotating medium or uniformly rotating medium a more spectacular picture emerges here, that is the break of slab symmetry which is a consequence of the MSI. Apparently, the initially straight flux tube has become significantly deformed. At one end of the y–domain the bulk of magnetic energy resides into two lengthy ropes separated by a distance $\approx H_0/2$ which coalesce at the other end to manifest in a fork–like appearance. Note that the spatial distribution of magnetic energy does not allow conclusions on the magnetic field topology. Indeed, Fig. 8 may indicate that the twisted magnetic tube has undergone numerical reconnection and is broken into two pieces at one side. But this is not necessarily the case here. The ropes are not magnetically isolated but embedded in a complex magnetic field topology.

The wake in the vicinity of the magnetic structure is characterized by a chaotic flow rather than showing a more ordered pattern like in the models before. The ordered velocity pattern seen at larger distance from the magnetic structure is initiated by sonic perturbations propagating upwards in the atmosphere. This flow is modified by the Coriolis force generating the observed pair of elongated, large–scale vortices. The average speed of rise is lower than in all previous cases. The vertical height of the magnetic structure remains below that in the uniformly rotating case at all times and reaches a maximum value $z_{\max} \approx 0.6$ at $t \approx 2.9$ (see Sect. 4.4 for a more detailed discussion).

The final stage of evolution ($t = 3.17$) for an untwisted flux tube is illustrated in Fig. 9. Although there are significant deformations of the tube's cross–section, no fully developed splitting of the flux tube is observed at this time. The magnetic structure still shows some degree of coherence, albeit it looks rather rumbled. Recall that in a non-rotating environment an untwisted flux tube is quickly disrupted and fragments into two halves which make out a vortex filament pair. The snapshot reflects the competing processes of destabilization due to differential buoyancy and external pressure forces and the stabilizing effect of rotation mediated by the Coriolis force. The subsequent fate of the magnetic structure is unclear. It is conceivable that during the later course of evolution the desintegration continues which, ultimately, leads to a breaking up into several pieces. It is found that, at later times ($t \gtrsim 1.4$), the rising speed is smaller compared to the twisted tube case and approaches an almost constant value. At the end

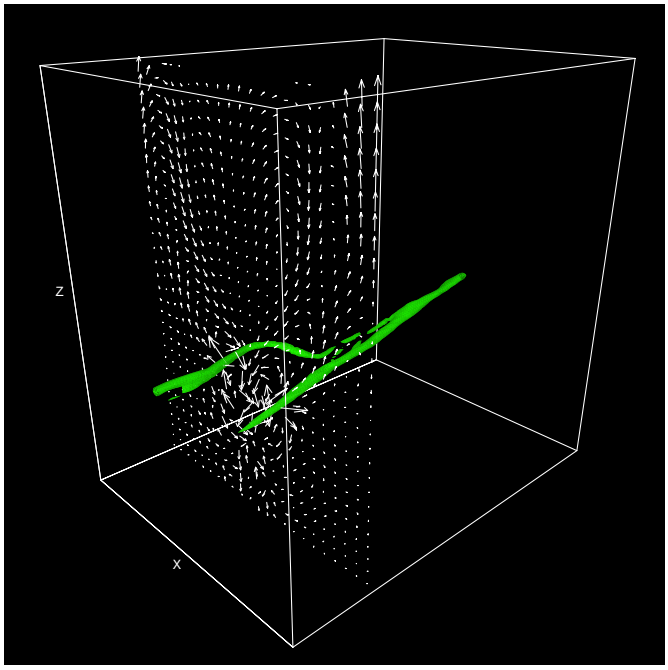

Fig. 8. Twisted tube case: isovolume of the magnetic field strength $|\boldsymbol{B}| = |\boldsymbol{B}|_{\max}/2$ and the transverse component of velocity in the plane $y = -0.6$ at time $t = 3.51$

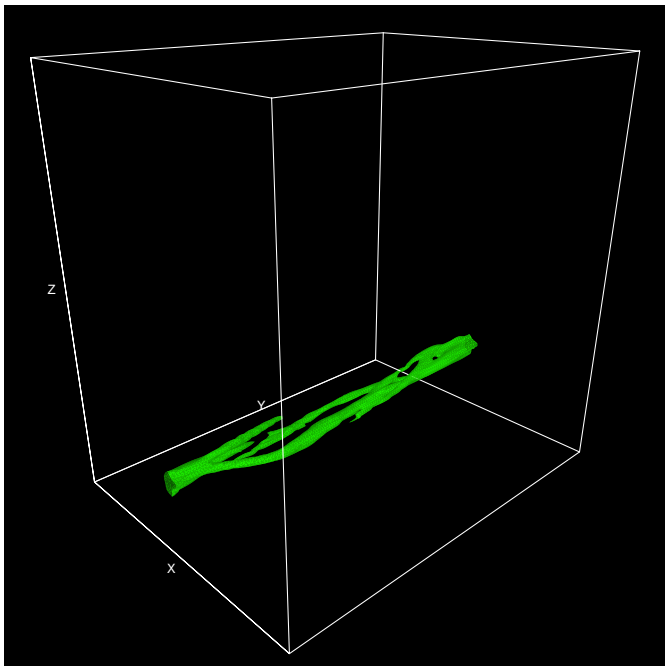

Fig. 9. Untwisted tube case: isovolume of the magnetic field strength $|\boldsymbol{B}| = |\boldsymbol{B}|_{\max}/2$ at time $t = 3.17$

of the simulation the magnetic structure has reached only a height $z \approx 0.34 \approx z_{\max}/2$.

4.4. Comparison with the thin flux tube approximation

In the TFA the rise of a straight, horizontal tube in a stratified medium with external density distribution $\rho_{\rm e}(z)$ is described by the equations:

$$\begin{aligned} \frac{\mathrm{d}z}{\mathrm{d}t} &= v_z, \\ 2\rho_{\rm e}\frac{\mathrm{d}v_z}{\mathrm{d}t} &= -(\rho-\rho_{\rm e})g - C_{\rm D}\frac{\rho_{\rm e}|v_z|v_z}{\pi R}, \end{aligned} \tag{5}$$

where $C_{\rm D}$ is the aerodynamic drag coefficient and R is the (z–dependent) radius of the flux tube. The factor $2\rho_{\rm e}$ in front of the acceleration term in the force equation is due to the enhanced inertia effect. Using the requirements of pressure balance, mass conservation, magnetic flux conservation, and an isothermal equation of state, one can determine the flux tube height as a function of time. Note that differential rotation with $\boldsymbol{\Omega} \parallel \hat{\boldsymbol{z}}$ does not alter the vertical motion of a thin flux tube. Thus, the above ansatz can be used equally well for the non–rotating case and rotating case.

For a comparison with the TFA, the vertical flux tube position in the numerical models is defined by the ($\boldsymbol{B}^2$–weighted) mean z–coordinate

$$\langle z\rangle(t) = \frac{\int z\boldsymbol{B}^2\mathrm{d}V}{\int \boldsymbol{B}^2\mathrm{d}V}. \tag{6}$$

Based on this definition the rising behavior for the various cases is monitored in Fig. 10. The curve labeled with letters "TFA" is computed from (5) using $C_{\rm D} = 2$ and an initial tube radius $R_0 = R(z = z_0)$ equal to the $\boldsymbol{B}^2$–weighted RMS radius of our initial flux tube i.e.

$$R_0 = \left(\frac{\int \left[x^2 + (z-z_0)^2\right]\boldsymbol{B}^2\mathrm{d}V}{\int \boldsymbol{B}^2\mathrm{d}V}\right)^{1/2}. \tag{7}$$

In the TFA the tube rises exponentially as expected under isothermal conditions and leaves the numerical domain after ≈2 orbits. Note that this result depends on the choice of $C_{\rm D}$. For subsonic flow and in the here relevant Reynolds number regime from ≈1 to ≈10^5 $C_{\rm D}$ is of the order of unity. In the 2D/3D non–rotating models the speed of rise is significantly lower than in the 1D TFA. This discrepancy is due to the large amount of magnetic flux lost to the wake. This loss leads to a drastic reduction of buoyancy in the flux tube and, thus, to a lower acceleration in z–direction.

As shown in Sect. 4.2 for the case of a uniformly rotating background medium the vertical motion of the flux tube is even more slowed down due to the action of the Coriolis force on the surrounding flow reacting upon the flux tube. Although this simulation has been stopped after 2.67 orbits, it is likely that the flux tube continues to rise and, extrapolating the given $\langle z\rangle$–profile, will reach the top of the domain after roughly 10 orbits.

In an accretion disk, the MSI acts as a very efficient braking mechanism for weakly twisted flux tubes. As a consequence the corresponding $\langle z\rangle$–curve (labeled by "Kepler rotation") lies below that of the uniformly rotating case. After the nonlinear stage of the instability sets in, that is after ≈3 orbits, the flux tube stops its vertical rise at a height of $z_{\max} \approx 0.6$. Later on, the tube speed

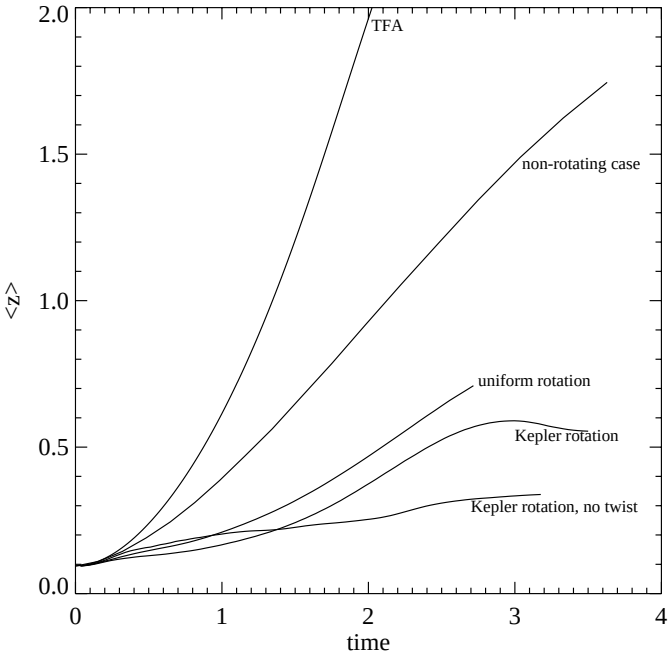

Fig. 10. Time dependence of the average vertical position of the magnetic structure for the various models

even changes sign and becomes negative. This explains the slight decrease of $\langle z \rangle$ for $t > 3$. Note that the "Kepler rotation" curve lies beneath all other curves for $t \lesssim 1.3$ because of the initial stretching effect of the twist field by the shear flow within the flux tube which leads to an increase in resistance.

The rise of an untwisted tube in a Kepler disk is mainly determined by two effects. The first is the tendency of the tube to fragment due to differential buoyancy and pressure forces like in the non–rotating models. The second concerns the stabilizing effect of the Coriolis force as explained in Sect. 4.2. Note that at this stage of development the MSI plays only a minor role because there is no initial poloidal field component which leads to rapid growth of the instability within the tube. In effect, the tube ascends rather slowly remaining even below $z_{\max}$ during the later course of evolution with no sign reversal of the rise velocity occurring.

5. Summary and conclusions

Using adaptive mesh simulations the evolution of buoyant flux tubes embedded in an isothermal non-rotating, uniformly rotating or differentially rotating atmosphere has been modeled. Simulations with slab symmetry (2D) and fully 3D simulations were performed.

If rotation is absent, the study shows that untwisted flux tubes quickly break–up into a pair of vortex filaments as a result of the differential buoyancy within the tube and the interaction of the tube with the external plasma. This behavior is reminiscent of numerical experiments of rising flux tubes in polytropic layers modeling the solar convection zone. Such tube splitting is not observed for a tube which possesses a weak twist field. This is because twist counteracts any deformation of the tube's cross–section by building up magnetic tension forces at the surface. However, because of the large pressure contrast between the bottom and top of isothermal atmosphere ($\approx$50), roughly 2/3 of the initial magnetic flux is peeled off the tube and is accumulated in two oppositely spinning large–scale eddies lagging behind the tube head. As a consequence of the drastic loss of magnetic flux the tube expands during its rise not as expected from flux conservation and the density stratification. By means of 3D simulations it has been further demonstrated that the weakly twisted, initially kink–stable flux tube remains kink–stable up to the finally reached height, although the critical pitch angle for the onset of the kink instability is passed over in a surface layer of the flux tube head. However, the inner region of the tube head is clearly stable which prohibits a full–blown instability.

The evolution of a weakly twisted flux tube changes if rotation is present. Significant differences are even found between the uniformly rotating case and differentially rotating case. In both the speed of rise of the magnetic structure is substantially reduced. The Coriolis force acts on the surrounding flow in a manner to increase the pressure difference between the front and back of the flux tube resulting in a downward directed force counteracting buoyancy. In case of Keplerian rotation the magnetic configuration is dynamically unstable due to the magnetic shear instability. As a consequence of the magnetic shear instability weakly twisted flux tubes are found to stop their vertical ascend at a maximum height $z \approx 0.6 H_0$. Hence, magnetic flux is possible stored a rather long time in the inner part of the disk ($z < H_0$) before it may enter into the disk corona. This finding is of relevance for disk dynamos. Many dynamo models critically depend on the amount of magnetic flux escaping from the disk due to buoyancy losses. If this loss is much larger than the rate at which magnetic flux can be regenerated through dynamo action, the dynamo mechanism cannot survive for a longer time than imposed by the buoyancy time scale. In light of the present results, however, the problem of buoyancy losses is much less severe or does not exist at all. The magnetic shear instability acting on the twisted tube provides a very efficient mechanism to suppress buoyancy. In case of an untwisted flux tube, the rise speed is also very small and, hence, the buoyancy time scale is large. Therefore, for both weakly twisted and untwisted flux tubes the expected magnetic flux escape in accretion disks due to buoyancy effects is small. The buoyant time scale are obtained in the limit of ideal electrical conductivity. Therefore, magnetic reconnection phenomena which might have some influence on the dynamics and, hence, on the details of buoyancy cannot occur physically. However, artificial (numerical) reconnection processes can lead to changes in the magnetic field topology if parallel magnetic field vectors of opposite sign are advected into one cell. To avoid such effects of artificial reconnection, models with finite electrical resistivity are required. Also, the effects of physical viscosity, radiation transfer and heat conduction have been ignored in

the present model. The inclusion of all these effects enormously increases the complexity of the problem and are beyond the scope of this research but remain a numerical challenge for future modeling.

It has been furthermore illustrated that the thin flux tube approximation is an inadequate tool to describe the evolution of buoyant flux tubes, if rotation with angular velocity vector parallel to the buoyancy force is a dynamically important factor. Especially, thin flux tube theory in those cases totally fails to predict the correct rising speed and vertical position of accretion disk flux tubes. For flux tube dynamo models based on thin flux tube approximation calculations this means that buoyancy losses can be rather overestimated. In a work of Hanasz & Lesch (1993) (see also Hanasz & Lesch 1997; Hanasz 1997) the scenario of a flux tube galactic dynamo has been investigated. They argued that the coefficient of turbulent diffusivity based on the characteristic velocity of rise of a flux tube can be decreased up to a factor of 10 and, hence, the dynamo number can be increased by a factor of 100. However, their conclusions are drawn on the basis of thin flux tube (1D) models. In 3D, as demonstrated in this paper, the speed of rise of isolated flux tubes is drastically reduced compared to thin flux tube models. Our results are thus in favor of even larger dynamo numbers. It must be noted, however, that our model so far does not consider the possibility of Parker modes. The Parker instability is another important ingredient and its effect is to be studied. Also, the simulations allow no conclusions for slow rotators like the Sun. The thin flux tube approximation may be still a useful tool for studying convection zone flux tubes at least under special physical conditions. In general, however, a self-consistent picture clearly requires high–resolution, three–dimensional simulations.

Acknowledgements. This work was financially supported by the DFG under grant UL 57/30-1. The computations were performed on workstations of the Institut für Theoretische Astrophysik, Universität Heidelberg, Germany.

References

Abramowicz, M., Brandenburg, A., & Lasota, J.-P. 1996, MNRAS, 281, L21
Balbus, S. A., & Hawley, J. F. 1991, ApJ, 376, 214
Balbus, S. A., & Hawley, J. F. 1992, ApJ, 400, 610
Brandenburg, A., Nordlund, Å., Stein, R. F., & Torkelsson, U. 1995, ApJ, 446, 741
Caligari, P., Moreno-Insertis, F., & Schüssler, M. 1995, ApJ, 441, 886
Dorch, S. B. F., & Nordlund, Å. 1998, A&A, 338, 329
Emonet, T., & Moreno-Insertis, F. 1996, ApJ, 458, 783
Emonet, T., & Moreno-Insertis, F. 1998, ApJ, 492, 804
Fan, Y., Fisher, G. H., & McClymont. A. N. 1994, ApJ, 436, 907
Fan, Y., Zweibel, E. G., Linton, M. G., & Fisher, G. H. 1998, ApJ, 505, L59
Fan, Y., Zweibel, E. G., & Lantz, S. R. 1998b, ApJ, 493, 480
Hanasz, M., & Lesch, H. 1993, A&A, 278, 561
Hanasz, M., & Lesch, H. 1997, A&A, 321, 1007
Hanasz, M. 1997, A&A, 327, 813
Hawley, J. F., Gammie, F., & Balbus, S. A. 1995, ApJ, 440, 742
Hawley, J. F., Gammie, F., & Balbus, S. A. 1996, ApJ, 464, 690
Hawley, J. F., & Stone, J. M. 1998, ApJ, 501, 758
Heiles, C. 1987, ApJ, 315, 555
Heiles, C. 1992, in Evolution of Interstellar Matter and Dynamics of Galaxies (Cambridge University Press)
Horiuchi, T., & Sato, S. 1993, PASJ, 42, 661
Hughes, D. W., & Falle, A. E. G. 1998, ApJ, 509, L57
Hughes, D. W. 1992, in Sunspots: Theory and Observations, ed. J. H. Thomas, & N. O. Weiss (Dordrecht: Kluwer), 371
Kleeorin, N. I., & Rogachevskii, I. V. 1990, Proceedings of ESA workshop SP–311 on Plasma Astrophysics held in Telavi, Georgia
Krause, F., & Rädler, K.-H. 1980, in Mean-Field Magnetohydrodynamics and Dynamo Theory (Pergamon Press)
Kutznetsov, V., & Hood, A. 1997, Solar Phys., 171, 61
Matthews, P., Hughes, D., & Proctor, M. 1995, ApJ, 448, 938
Moreno-Insertis, F., & Emonet, T. 1996, ApJ, 472, L53
Linton, M. G., Dahlburg, R. B., Fisher, G. H., & Longcope, D. W. 1998, ApJ, 507, 404
Longcope, D., Fisher, G., & Arendt, S. 1996, ApJ, 464, 999
Parker, E. N. 1974, ApJ, 191, 245
Saffman, P. G. 1992, Vortex Dynamics (Cambridge: Cambridge Univ. Press), chap. 3
Schramkowski, G. P., & Achterberg, A. 1994, Space Sci. Rev., 68, 331
Schüssler, M. 1979, A&A, 71, 79
Sheeley, N. R. 1992, in The Solar Cycle, Astron. Soc. Pac. Conf. Ser., 27, 1
Stone, J. M., Hawley, J. F., Gammie, C. F., & Balbus, S. A. 1996, ApJ, 463, 656
Ulmschneider, P., Zähringer, K., & Musielak, Z. E. 1991, A&A, 241, 625
van Breugel, & W., Formalont, E. B. 1984, ApJ, 282, L55
Wang, Y.-M., & Sheeley, N. R. 1991, ApJ, 375, 761
Wang, Y.-M., Zirin, H., & Ai, G. 1991, Solar Phys., 131, 53
Weiss, N. O. 1994, in Lectures on Solar and Planetary Dynamos, ed. M. R. E. Proctor, & A. D. Gilbert (Cambridge: Cambridge Univ. Press), 59
Ziegler, U., & Yorke H. W. 1997, Comp. Phys. Comm., 101, 54
Ziegler, U. 1998, Comp. Phys. Comm., 109, 111
Ziegler, U. 1999, Comp. Phys, Comm., 116, 65
Ziegler, U., & Rüdiger, G. 2000, A&A, 356, 1141